

# HiLumi LHC

FP7 High Luminosity Large Hadron Collider Design Study

## Deliverable Report

# Design of the NB3SN Inner Triplet

Cavanna, E (CERN) *et al*

04 September 2015



The HiLumi LHC Design Study is included in the High Luminosity LHC project and is partly funded by the European Commission within the Framework Programme 7 Capacities Specific Programme, Grant Agreement 284404.

This work is part of HiLumi LHC Work Package 3: **Magnets for Insertion Regions**.

The electronic version of this HiLumi LHC Publication is available via the HiLumi LHC web site <<http://hilumilhc.web.cern.ch>> or on the CERN Document Server at the following URL: <<http://cds.cern.ch/search?p=CERN-ACC-2015-0093>>

Grant Agreement No: 284404

# HILUMI LHC

FP7 High Luminosity Large Hadron Collider Design Study

Seventh Framework Programme, Capacities Specific Programme, Research Infrastructures,  
Collaborative Project, Design Study

## DELIVERABLE REPORT

# DESIGN OF THE $Nb_3Sn$ INNER TRIplet

**DELIVERABLE: D3.2**

---

<b>Document identifier:</b>	HILUMILHC-Del-D3-2-v1.0
<b>Due date of deliverable:</b>	End of Month 48 (October 2015)
<b>Report release date:</b>	04/09/2015
<b>Work package:</b>	WP3 IR Magnets
<b>Lead beneficiary:</b>	CERN
<b>Document status:</b>	Final

---

### Abstract:

The High Luminosity LHC (HL-LHC) project is aimed at implementing the necessary changes in the LHC to increase its integrated luminosity by a factor ten. Among the magnets that will be replaced are the 16 superconducting inner triplet (low- $\beta$ ) quadrupoles placed around the two high luminosity interaction regions (ATLAS and CMS experiments). The new quadrupole magnets will have to generate a gradient of 132.6 T/m in a coil aperture of 150 mm. The resulting conductor peak field of about 12 T will require the use of  $Nb_3Sn$  superconducting coils. We present in this document the design HL-LHC low- $\beta$  quadrupole magnets, called MQXF, focusing in particular on superconductor characteristics, coil lay-out, support structure concept, and quench protection system.

Copyright notice:

Copyright © HiLumi LHC Consortium, 2015.

For more information on HiLumi LHC, its partners and contributors please see [www.cern.ch/HiLumiLHC](http://www.cern.ch/HiLumiLHC)

The HiLumi LHC Design Study is included in the High Luminosity LHC project and is partly funded by the European Commission within the Framework Programme 7 Capacities Specific Programme, Grant Agreement 284404. HiLumi LHC began in November 2011 and will run for 4 years.

The information herein only reflects the views of its authors and not those of the European Commission and no warranty expressed or implied is made with regard to such information or its use.

### Delivery Slip

	<b>Name</b>	<b>Partner</b>	<b>Date</b>
<b>Authored by</b>	E. Cavanna, P. Ferracin, S. Izquierdo Bermudez, M. Juchno, J.C. Perez, E. Todesco	CERN	12/06/2015
	G. Ambrosio, R. Bossert, G. Chlachidize, L.D. Cooley, E.F. Holik, V.V. Kashikhin, S. Krave, F. Nobrega, I. Novitski, M. Yu1, A.V. Zlobin	FNAL	
	M. Anerella, A. Ghosh, J. Muratore, J. Schmalzle, P. Wanderer	BNL	
	F. Borgnolutti, D. Cheng, D. Dietderich, H. Felice, A. Godeke, R. Hafalia, M. Marchevsky, S. Prestemon, G.L. Sabbi, X. Wang	LBNL	
<b>Edited by</b>	C. Noels	CERN	16/07/2015
<b>Reviewed by</b>	L. Rossi, Project Coordinator	CERN	19/07/2015
<b>Approved by</b>	Steering Committee		03/09/2015

## TABLE OF CONTENTS

<b>1. INTRODUCTION</b>	<b>4</b>
<b>2. CONDUCTOR CHARACTERISTICS</b>	<b>4</b>
2.1. STRAND CHARACTERISTICS	4
2.2. CABLE CHARACTERISTICS	5
2.3. CABLE INSULATION	6
<b>3. MAGNETIC DESIGN</b>	<b>6</b>
3.1. 2D MAGNETIC DESIGN	6
3.1.1. Coil main parameters	6
3.1.2. ROXIE model	8
3.1.3. Magnet performance	8
3.1.4. Field quality	10
<b>4. 3D MAGNETIC DESIGN</b>	<b>12</b>
4.1. DESIGN OBJECTIVES AND PROCESS	12
4.2. STUDY OF PEAK FIELD ENHANCEMENT	14
4.3. STUDY OF INTEGRATED FIELD HARMONICS	14
4.4. MAGNETIC AND PHYSICAL LENGTHS	15
<b>5. COIL DESIGN AND PARTS</b>	<b>17</b>
<b>6. STRUCTURE DESIGN AND INSTRUMENTATION</b>	<b>19</b>
6.1. DESIGN CONCEPT	19
6.2. 2D ANALYSIS	21
6.3. 3D ANALYSIS	21
6.3.1. Shell segmentation	21
6.4. MAGNET ASSEMBLY	22
<b>7. QUENCH PROTECTION</b>	<b>22</b>
7.1. HEATER DESIGN	23
7.1.1. Copper-plated heater design 1 (IL)	23
7.1.2. Copper-plated heater design 2 (IL/OL)	24
7.2. TRACE FABRICATION	26
7.3. CLIQ	27
7.4. ANALYSIS	28
<b>8. CONCLUSIONS</b>	<b>29</b>

## Executive summary

*We present in this document the design of the HL-LHC low- $\beta$  quadrupole magnets, called MQXF, focusing in particular on superconductor characteristics, coil lay-out, support structure concept, and quench protection system.*

## 1. INTRODUCTION

The present Interaction Regions (IR) of the Large Hadron Collider [1] include four single-aperture quadrupole magnets (called low- $\beta$  or inner triplet quadrupoles) based on Nb-Ti superconducting technology [2]. These quadrupoles present two different designs, both with an aperture of 70 mm and an operating gradient of 205 T/m: MQXA [3], developed by KEK, with a magnetic length of 5.5 m, and MQXB [4], built at FNAL, with a magnetic length of 6.37 m. With the current IR design, the LHC is expected to reach its nominal luminosity of  $10^{34}$  cm<sup>-2</sup> s<sup>-1</sup> and to provide  $\sim 300$  fb<sup>-1</sup> of integrated luminosity by 2022. By replacing the current triplets with a new quadrupole design with an aperture of 150 mm and based on Nb<sub>3</sub>Sn technology, the HL-LHC Project aims to increase the peak luminosity by a factor of 5 and reach 3000 fb<sup>-1</sup> of integrated luminosity. The new quadrupole magnets, called MQXF, will be developed by a joint effort of LARP, a collaboration between three US laboratories (BNL, FNAL and LBNL), and CERN. The purpose of this document is to give an overview of the MQXF design and parameters.

At the time of the submission of this document, the first MQXF short model, called MQXFS1, with a magnetic length of 1.2 m, has been fabricated and is in the process of being assembled. The test is expected by the end of 2015. All the parameters and images of this document refer to the design of MQXFS1. The final magnets to be installed in the LHC, MQXFA and MQXFB, respectively 4.2 and 7.15 m long, will be a length scale-up of the short model.

## 2. CONDUCTOR CHARACTERISTICS

The Rutherford cable for the MQXFS magnets is fabricated using 40 Nb<sub>3</sub>Sn strands of diameter 0.85 mm. The strand is either a Rod-Restack-Process RRP® strand manufactured by Oxford-Instrument Superconducting Technology or a Powder-In-Tube PIT strand produced by Bruker Energy & Supercon Technologies (BEST). The coils fabricated by LARP will use RRP conductor, whereas those made by CERN will use both RRP and PIT conductors.

### 2.1. STRAND CHARACTERISTICS

The cable for the MQXFS1 magnet will be fabricated using the RRP Nb<sub>3</sub>Sn wire. Strand diameter is 0.85 mm. The 108/127 layout (being 108 the actual number of Nb<sub>3</sub>Sn filaments) with Ti-doping will be utilized. Ti-doping is introduced by replacing a few Nb rods in the sub-element with rods of Nb-Ti. The main characteristics of the strands are summarized in Table I. According to the specifications, the strand will have a critical current in the superconductor of 2450 A/mm<sup>2</sup> at 12 T and 4.2 K, and of 1280 A/mm<sup>2</sup> at 15 T and 4.2 K. the Cu/Sc ratio is 1.2. The reaction used by OST to qualify the strand before delivery of strand to LARP is 210°C/48 hr + 400°C/48 hr + 650°C/50 hr. To increase the manufacturing margin and increase RRR, the tin content in the sub-element core was reduced by 5% from the standard amount. The wires from these “Reduced-Sn” billets showed a marked increase in RRR to values over 300. Since coils for MQXFS will use wires from both standard and reduced tin, the reaction at the high temperature will be restricted to 640°C/48 hr.

**TABLE I: MAIN PARAMETERS OF THE 108/127 STRAND**

	unit	
Process		Ti-Ternary RRP Nb <sub>3</sub> Sn
Strand Diameter	mm	0.85 ± .003
I <sub>c</sub> (12 T) at 4.2 K, A	A	> 632
I <sub>c</sub> (15 T) at 4.2 K, A	A	> 331
J <sub>c</sub> (12 T) at 4.2 K	A/mm <sup>2</sup>	> 2450
J <sub>c</sub> (15 T) at 4.2 K	A/mm <sup>2</sup>	> 1280
D <sub>s</sub> , (sub-element diameter)	μm	< 55
Cu/Sc ratio		1.2 ± 0.1
RRR (after full reaction)		≥ 150
Twist Pitch	mm	19 ± 3
Twist Direction		right-hand screw
Minimum Piece length	m	550
High temperature HT duration	h	≥ 40

**TABLE II: MAIN PARAMETERS OF THE CABLE**

	unit	
Number of Wires in Cable		40
Cable Mid-Thickness	mm	1.525 ± 0.010
Cable Width	mm	18.15 ± .05
Cable Keystone Angle	degrees	0.55 ± 0.1
Cable Lay Direction		Left
Cable Lay Pitch	mm	109 ± 3
Stainless Steel Core Width	mm	12
Core Thickness	mm	0.025
Maximum Cable Residual Twist	degrees	+ 150
Cabling J <sub>c</sub> degradation	%	5
RRR (after full reaction)		≥ 100

## 2.2. CABLE CHARACTERISTICS

The MQXFS cable will use 40 strands and have a minimum coil unit length of 150 m, corresponding to about 40 kg of wire. The cable R&D was focused on minimizing the number of sheared sub-elements and the critical current cabling degradation. The cable dimensions provide in Table II are: a width of 18.15 ± 0.05 mm, a mid-thickness of 1.525 ± 0.010 mm, and a keystone angle of 0.55 ± 0.10 degrees. A reduction of the keystone angle to 0.4 degrees will be applied to the cable for the second generation coils, in order to reduce further performance degradation after cabling. A stainless steel core 25 microns thick and 12 mm wide is incorporated in the cable to reduce dynamic effects. Each cable unit length is accepted for coil winding after examining the minor edge compaction by light microscopy for strand damage, and evaluating I<sub>c</sub>, and RRR values of extracted strands that are reacted using the MQXFS-heat-treatment schedule.

## 2.3. CABLE INSULATION

The 18 mm wide keystone cable fabricated will be insulated by braiding S-2 glass fiber directly on the cable using an appropriate braiding machine. The cable is insulated by braiding the glass yarn using a 48 carrier braiding machine. The insulation material shall be S-2 Glass fiber, 2-ply yarn, produced by AGY with 933 sizing. The nomenclature for the glass being applied to the cable is SCG 75 2/0 0.3S. The insulation thickness is specified to be 0.145 mm  $\pm$  0.005 mm as determined by a 10-stack measurement at 5 MPa.

## 3. MAGNETIC DESIGN

### 3.1. 2D MAGNETIC DESIGN

#### 3.1.1. Coil main parameters

The cross-section of the MQXF coil is shown in Fig. 1. It is based on the  $\cos 2\theta$ -type design. With four blocks of conductor (two blocks per layer) the coil has enough free parameters to fine tune the multipoles (angular position) while keeping a low complexity in the winding. Besides providing a large gradient and a field quality within specifications, the selected coil also features:

- a total number of turns (50) close to the maximum one can get for this coil layout
- a peak stress due to azimuthal magnetic force about the same in both layers.
- a coil layout that is very similar to the 120 mm aperture HQ quadrupole (see Fig. 3 where HQ and QXF coil cross-sections are superimposed). This is a valuable feature as the experience in Nb<sub>3</sub>Sn coil fabrication gained with HQ will be directly transferred to MQXF.

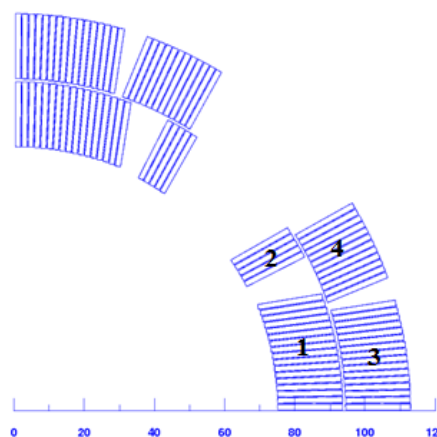


Fig. 1. Cross-section of the QXF\_v1 coil.

More information about the selection of the coil cross-section can be found in [5]. The MQXF coil main parameters are summarized in Table III. Dimensions of the cable before and after reaction are both given but only the dimension of the reacted cable is used for the calculations. After reaction the cable is assumed to have its thickness and width increased by 4.5% and 2%, respectively.

TABLE III: MAIN PARAMETERS OF THE MQXF COIL.

	unit	
Coil aperture radius	mm	75.000
Layer 1 outer radius	mm	93.813
Inter-layer insulation thickness	mm	0.500
Outer layer inner radius	mm	94.313
Outer layer outer radius	mm	113.126
Mid-plane shim thickness (per coil)	mm	0.250
Number of turns in block 1		17
Number of turns in block 2		5
Number of turns in block 3		12
Number of turns in block 4		6
Bare unreacted/reacted conductor width	mm	18.150/18.513
Bare unreacted/reacted conductor thickness	mm	1.525/1.594
Keystone angle	deg	0.55
Insulation thickness	mm	0.150

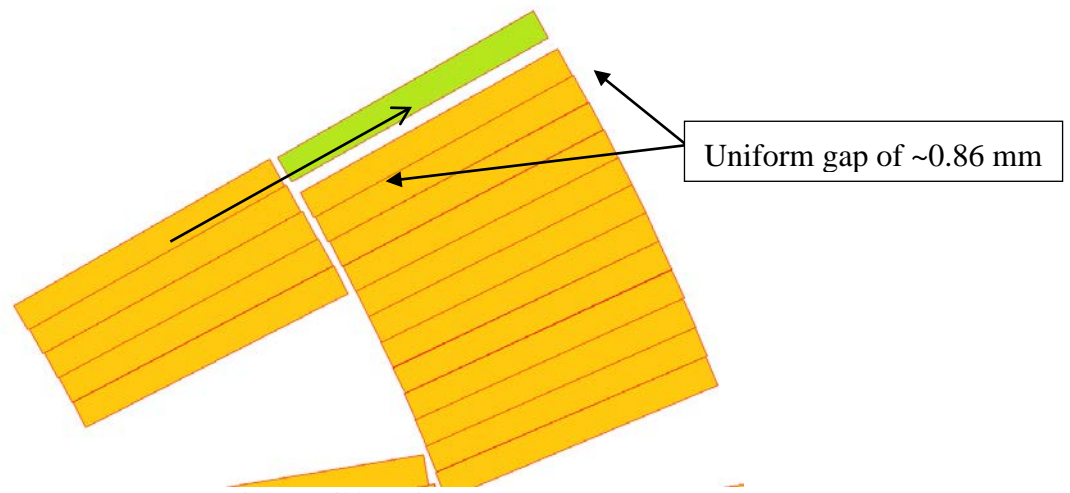


Fig. 2. Coil layer jump.

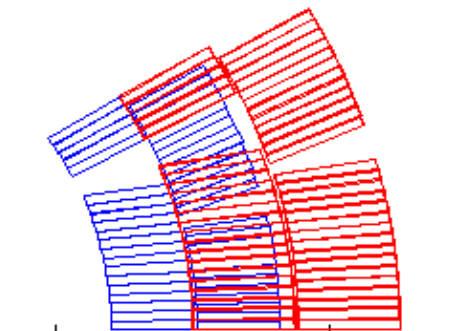


Fig. 3. Cross-section of the MQXF coil (red) superimposed to the cross-section of the HQ coil. Both MQXF and HQ feature a similar coil layout.

The relative position of the block number 2 and 4 (top block of layer 1 and top block of layer 2) is such that the broad face of the layer jump turn (green conductor) is parallel to the broad face of the top conductor of the upper block outer layer (see Fig. 2). This way a rectangular shim (~0.86 mm) can be used.



### 3.1.2. ROXIE model

The computation of the magnetic field was performed with the ROXIE software [6]. In Fig. 4 the 2D data table as implemented in ROXIE is given. As for HQ design, the option “alignment of the conductor on the coil OD” was selected (ODFAC = 1). Practically, this reflects the fact that the coil has the tendency to move away from the winding mandrel after winding (spring back), as seen from practice coil cross section.

Block Data 2D											
No	Type	NCab	X	Y	$\alpha$	Current	Cable name	N1	N2	Imag	Turn
1	Cos	17	75	0.19099	0	16479	XF150HT	2	20	0	0
2	Cos	5	75	28	27	16479	XF150HT	2	20	0	0
3	Cos	16	94.313	0.15188	0	16479	XF150HT	2	20	0	0
4	Cos	12	94.313	18.95	22.6	16479	XF150HT	2	20	0	0

Fig. 4. Input-file of the QXF coil used in ROXIE.

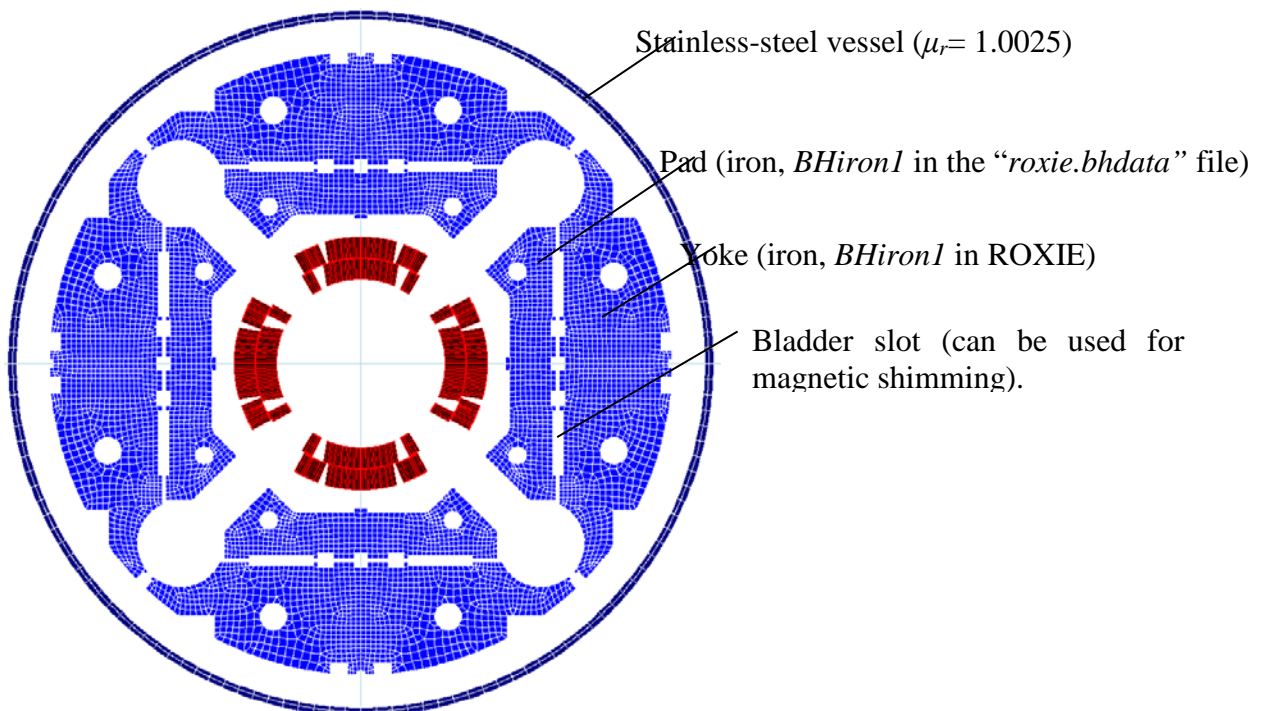


Fig. 5. MQXF magnet model used in ROXIE.

In the MQXF assembly the superconducting coil is surrounded by iron pads and yokes which reinforce the field in the aperture and reduce the stray field outside the magnet. These elements are also integral components of the shell-based support structure. As a consequence the yoke and the pad implement slots for the insertion of the bladders and groves for the keys. The 2D FEM model used for the computation of the magnetic field is shown in Fig. 5. The *BH* characteristic used for the iron components is defined as “BHiron1” in the *roxie.bhdata* file. This *BH* curve assumes a filling factor of 1 (full body). Note that no thermal contraction factor was used for the computation of the harmonics, *i.e.*, the coil is assumed to be at room temperature. The impact of cool-down and mechanical deformation on field quality will be discussed in session 3.1.4.1.

### 3.1.3. Magnet performance

Minimal requirements for wire manufacturing set by CERN and LARP require a critical current larger than 632 A and 331 A in respectively 12 T and 15 T applied field and at a

temperature of 4.2 K. For the computation of the magnet short sample current 5% degradation on the current due to cabling is assumed. In addition, to define the final critical curve, a correction factor of 0.429 T/kA is used to take into account the strand self-field. It corresponds to the magnetic field produced at 89% of the radius of a straight wire. For the characterization of the critical surface the scaling law developed in [7] is used. In Table IV the magnetic parameters of the MQXF magnet when powered at short sample ( $I_{ss}$ ) and nominal ( $I_{nom}$ ) currents are given (see fig. 6). The operational temperature of the MQXF magnet is 1.9 K. The maximum current ( $I_{max}$ ) is set to 8% more than of  $I_{nom}$ , following the HL-LHC project guidelines. In Fig. 7 the magnetic field density in the coil (left) and in the yoke (right) at nominal current are plotted. At  $I = I_{nom}$  the peak field in the coil reaches 11.42 T. The peak field is located in the upper block of the inner layer (block 2). The proximity of the yoke with the coil results in a highly saturated iron yoke that translate in a ~9% reduction in the transfer function at nominal current (see Fig. 8-left). For the same reason the differential inductance  $L_d$  is non-linear (see Fig. 8-right). In spite of being highly saturated the iron yoke still contribute to enhancing the magnet gradient by ~ 8% at  $I_{nom}$  (from 121.7 T/m to 132.6 T/m).

TABLE IV: MAINS MAGNETIC PARAMETERS OF THE MQXF CROSS-SECTION CONSIDERING AN OPERATIONAL TEMPERATURE OF 1.9 K.

	unit	$I_{ss}$	$I_{max}$	$I_{nom}$
% of $I_{ss}$	%	100	83	77
Current	kA	21.52	17.90	16.48
Gradient	T/m	170.1	143.2	132.6
Peak field	T	14.66	12.33	11.42
Temperature margin	K	0	3.8	4.9
Fx per octant	MN/m	3.92	2.80	2.48
Fy per octant	MN/m	-5.83	-4.21	-3.49
Energy	MJ/m	1.92	1.37	1.06
$L_d$	mH/m	8.13	8.18	8.23

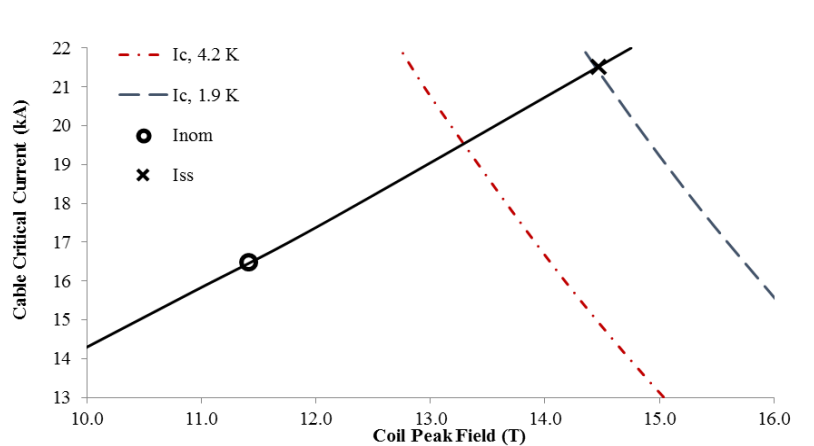


Fig. 6. MQXF quadrupole load line (current in the cable versus peak field in the coil). The peak field is always located in block 2. The load line has been obtained by gradually increasing the current in the coil. This way the non-linearity of the load line is taken into account. The critical surface accounts for 5% current degradation and for self-field correction.

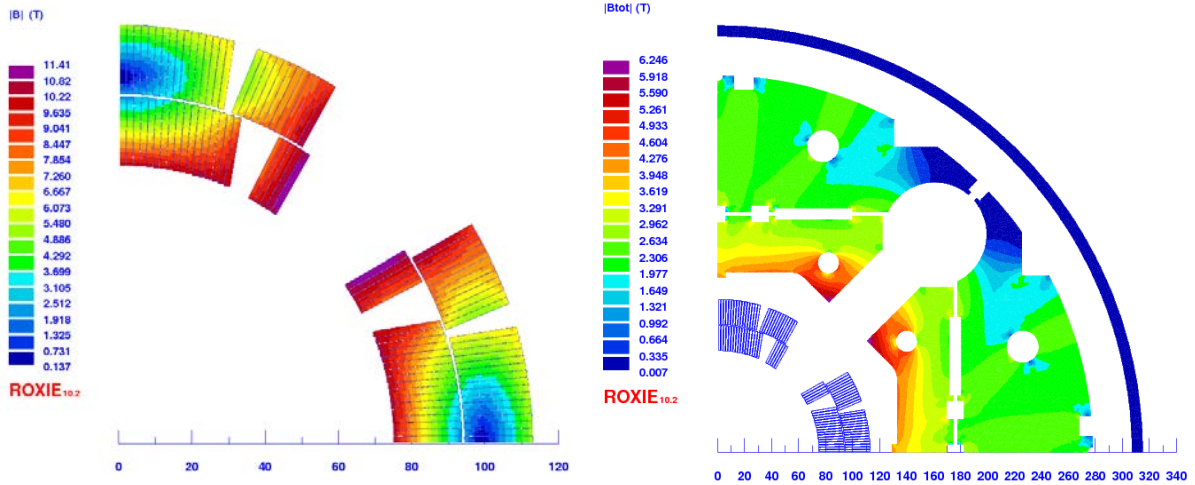


Fig. 7. Magnetic flux density in the coil (left) and in the yoke (right) at nominal current ( $I_{nom}$ ).

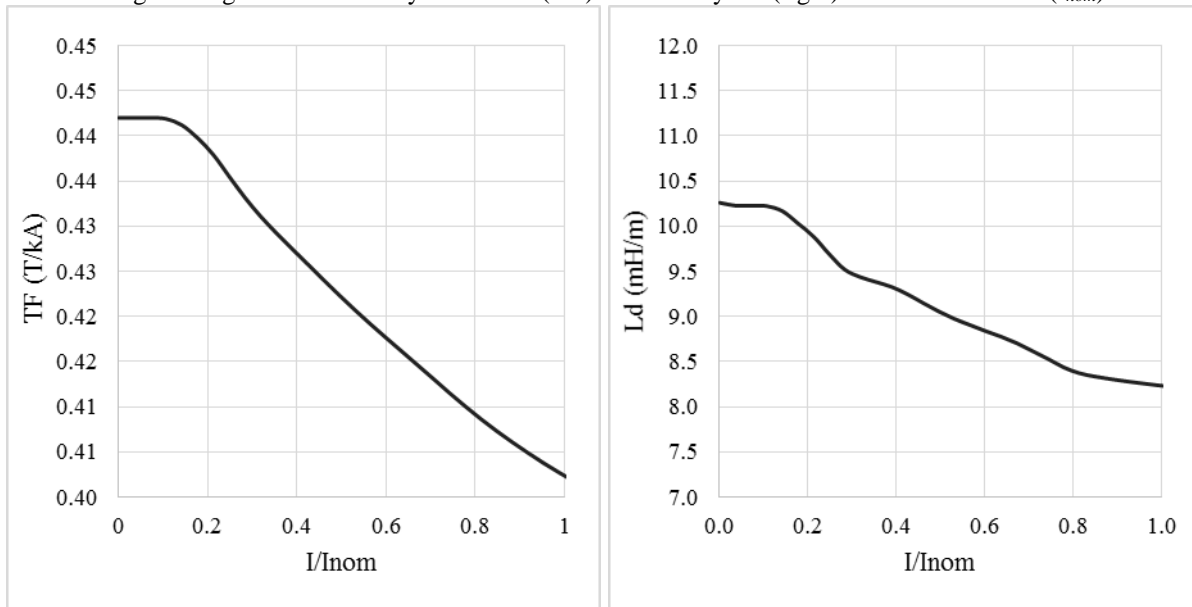


Fig. 8. Left: Transfer function defined as  $B_2(R_{ref}, I)/I$  and expressed in [T/kA] plotted versus  $I/I_{nom}$ . Right: differential inductance  $L_d$  in mH/m. Roxie was used for the computations.

### 3.1.4. Field quality

Regarding the magnetic field in the magnet aperture it was required that all allowed harmonics are within one unit at nominal current and at a reference radius taken as 2/3 of the coil aperture radius ( $R_{ref} = 50$  mm). The following convention for the definition of the multipoles is used:

$$B_y + iB_x = 10^{-4} B_2 \sum_{n=1}^{\infty} (b_n + ia_n) \frac{(x + iy)^{n-1}}{R_{ref}^{n-1}}$$

The evolution of the first four allowed harmonics ( $b_6$ ,  $b_{10}$ ,  $b_{14}$  and  $b_{18}$ ) with the current is plotted in Fig. 9. Numerical values of the field components calculated for  $I_{ss}$ ,  $I_{max}$  and  $I_{nom}$  are given in Table V.

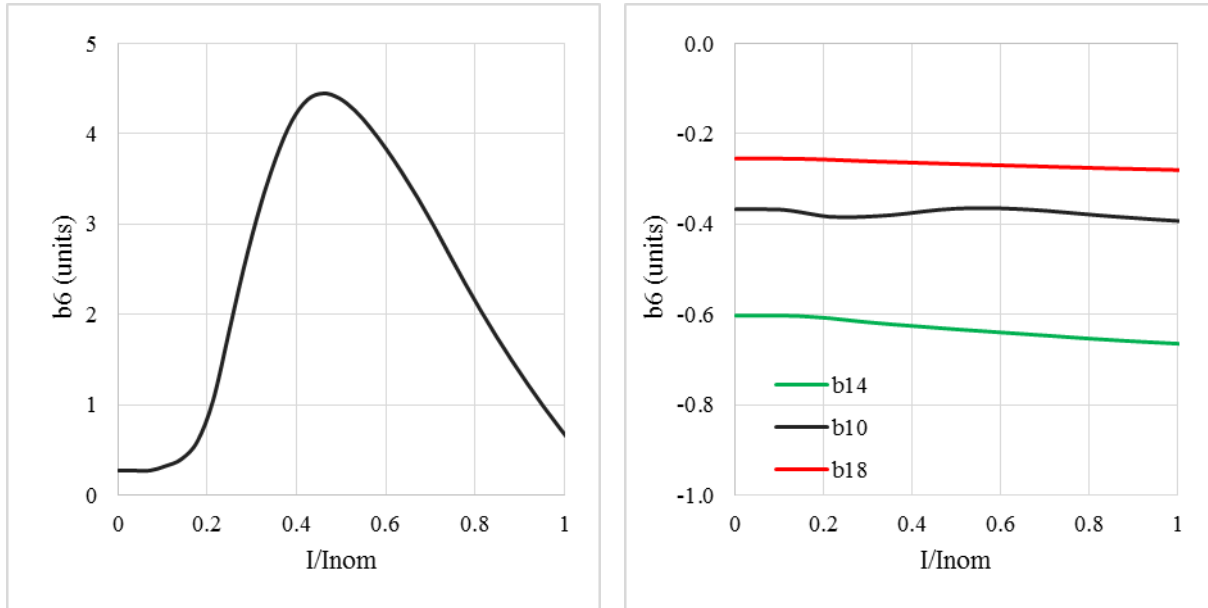


Fig. 9. First four allowed harmonics ( $b_6$ ,  $b_{10}$ ,  $b_{14}$  and  $b_{18}$ ) plotted versus the  $I/I_{nom}$  ratio. Harmonics are expressed in units.

TABLE V: FIELD HARMONIC COMPONENTS CALCULATED FOR  $I_{ss}$ ,  $I_{MAX}$  AND  $I_{NOM}$ .

	unit	$I_{ss}$	$I_{max}$	$I_{nom}$
% of $I_{ss}$	%	100	83	77
Current	kA	21.52	17.90	16.48
Gradient	T/m	170.09	143.2	132.60
$b_6$	unit	-0.87	0.16	0.68
$b_{10}$	unit	-0.41	-0.40	-0.39
$b_{14}$	unit	-0.68	-0.67	-0.66
$b_{18}$	unit	-0.28	-0.28	-0.28

### 3.1.4.1. Systematic field error

Field calculations are performed assuming that conductors are aligned on their OD as it seems to be the natural position of the turns (spring back). However, it is clear that one do not totally control the position of the cable in the impregnation cavity. Therefore, for completeness, in Table VI it is also given multipoles for the case where conductors are aligned on the ID. The current is set to  $I_{nom}$ .

TABLE VI: ALLOWED HARMONICS AT NOMINAL CURRENT AND WITH TURNS EITHER ALIGNED ON THE COIL OD (BASELINE) OR ID.

Multipoles	Turns aligned on the coil OD (baseline)	Turns aligned on the coil ID
$b_6$	0.68	-0.76
$b_{10}$	-0.39	-0.98
$b_{14}$	-0.66	-0.65
$b_{18}$	-0.28	-0.26

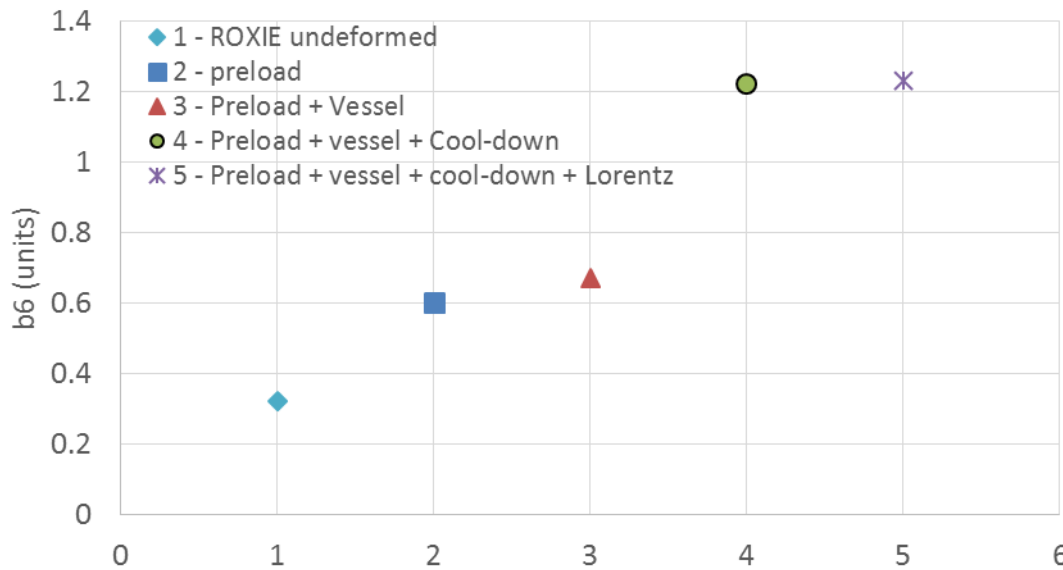


Fig. 10. Impact coil deformations due to cool-down, pre-loading, and energizing on  $b_6$ .

Another source of systematic error is the deformation of the coil after cool down due to thermal contraction and pre-load of the coil (see Fig. 10). The results of the 2D structural analysis in ANSYS were used to investigate the effects of the coil deformation on the field quality. The study was carried out by importing the coil displacement map extracted from the ANSYS solution into the 2D magnetic model implemented in Roxie. The displacement map corresponds to the state of the coil after the room temperature pre-load, the cool-down and the excitation to  $I_{nom}$ , and it is estimated with respect to the design coil geometry at room temperature without any pre-load. The computed displacements were applied to every strand of the magnetic model and a harmonic analysis was performed with the displaced strand distribution. The deformation of the iron yoke was not taken into account during this analysis. The results of the mechanical analysis indicate a radial displacement of the blocks of -0.3 to -0.4 mm and an azimuthal displacement of -0.04 to -0.05 mm. The output of the numerical magnetic model showed a change in the normalized  $b_6$  harmonic of about 0.9 units and a negligible change of other allowed harmonics such as  $b_{10}$  and  $b_{14}$ . The offset of the  $b_6$  is mostly caused by the azimuthal coil deformation, which results from the pre-load applied to the structure during the assembly and the structure contraction during the cool-down phase. As expected for quadrupole magnets, the deformations resulting from the electro-magnetic forces have a negligible effect on the  $b_6$ .

## 4. 3D MAGNETIC DESIGN

### 4.1. DESIGN OBJECTIVES AND PROCESS

From the magnetic point of view, the design objectives for coil ends optimization are:

- 1) to limit the peak field enhancement in the ends;
- 2) to keep the coil end as compact as possible in order to increase the magnetic length for a given coil length;
- 3) to minimize the multipole content of the integrated field.

In the case of MQXF, coil end optimization has been carried out in two stages. First of all, a preliminary magnetic analysis was done in ROXIE, focusing on the reduction of the peak

field and field errors. As a result, the number of blocks in the ends and the longitudinal spacing between coil blocks was fixed.

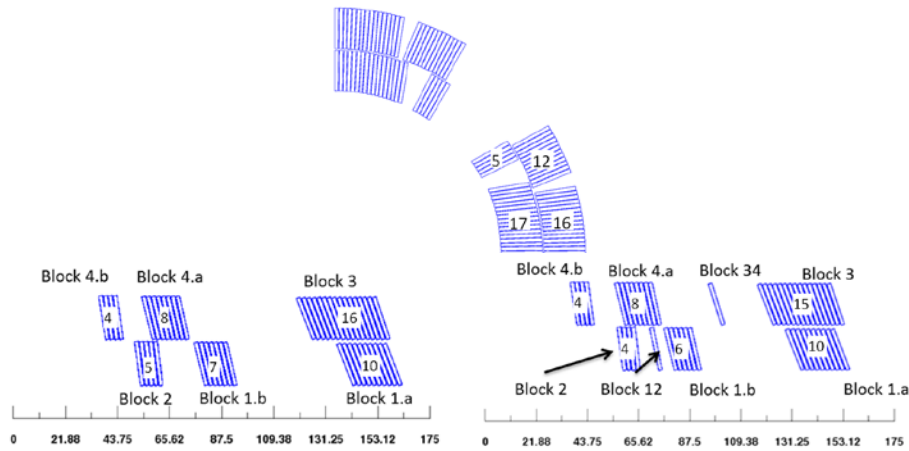


Fig. 13. Number of conductors per block

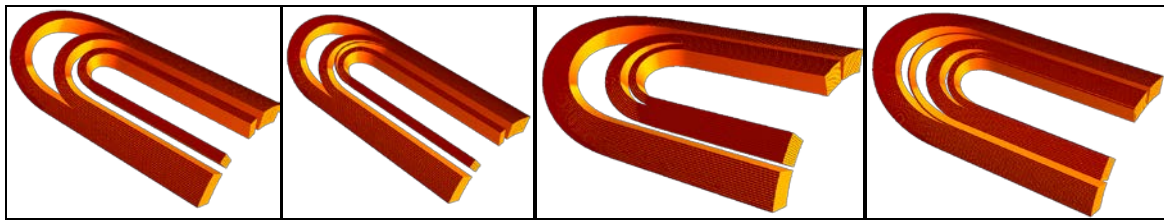
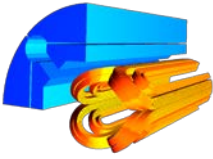
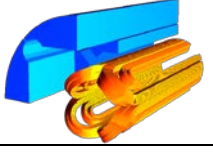
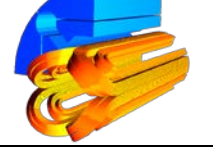


Fig. 14. Detail of the coil geometry

TABLE VII: CHANGE ON THE 3D PEAK FIELD AND MAGNETIC LENGTH FOR DIFFERENT MAGNETIC PAD AND YOKE

		$\Delta B_p$		$\Delta l_m$
		[T]	[%]	[mm]
Full iron pad and yoke		0.31	3	0
Pad shortened by 170 mm <u>(Selected design)</u>		-0.15	-1.3	-17.8
Pad & yoke shortened by 170 mm		-0.34	-2.9	-22.5

In a second stage, geometrical and mechanical optimization was performed at FNAL and CERN using different tools. FNAL uses the software BEND; CERN uses ROXIE. Both programs are based on differential geometry methods. During this second step of the

optimization process, coupled with winding tests, we focused on reducing the gaps between cable and spacers. Different lay-outs were studied; the final choice considers the subdivision of the coil blocks in the ends due to the better capability to reduce the integrated field harmonics and the lower peak field enhancement on the ends. Fig. 13 shows the blocks subdivision for MQXFS1 end design. Fig.14 shows a 3D detailed view of the ends. From left to right, the first image corresponds to the inner layer return end, the second to the inner layer lead end, the third to the outer layer return end and the last corresponds to the outer layer connection end.

#### 4.2. STUDY OF PEAK FIELD ENHANCEMENT

The aim of the optimization process is to guarantee that the maximum field in the coil ends is lower than the peak field in the straight section. This is achieved by an adequate placing of the blocks at the end and by partially removing the magnetic iron in the end region. As described in [9], the mechanical structure presently considered for MQXF is a shell-based structure. Iron yoke and pad are independent so a possible solution is to shorten only the pad. A study was carried out to determine the optimal cut-back length of the magnetic iron, which is a compromise in between the reduction of the magnetic length and the decrease of the peak field in the ends. Table VII presents the relative change on peak field in the ends with respect to the straight section for the cases where the pad and yoke are full length, if the yoke is full length and the pads are short and if both yoke and pads are short. Fig. 15 shows the peak field in the ends as a function of the arc length of the conductor for the final design, where the magnetic yoke is full length and only the magnetic pad is shortened.

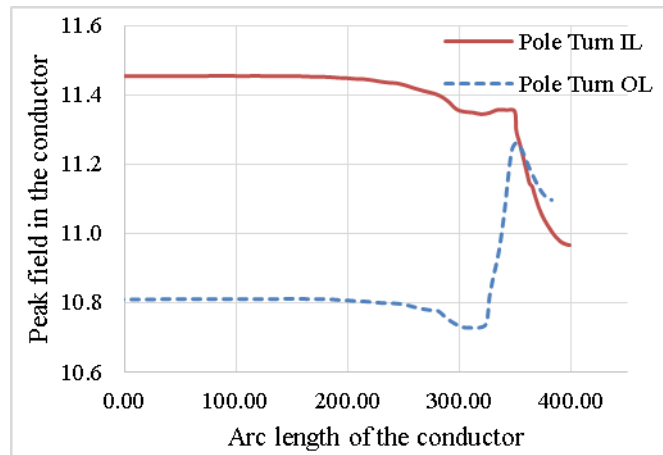


Fig. 15. Peak field enhancement in the return end

#### 4.3. STUDY OF INTEGRATED FIELD HARMONICS

The objective is to have an integrated multipole content lower than the random components, defining the integrated multipole content as

$$\bar{b}_n = \frac{\int_{-\infty}^{+\infty} B_n(I, z) dz}{B_2^{ss} l_{mag}(I)} \quad (1)$$

where  $B_n$  follows the convention

$$B_y + iB_x = \sum (B_n + iA_n)(x + iy)^{n-1}, \quad (2)$$

$B_2^{ss}$  is the main field in the straight section and  $l_{mag}$  is the magnetic length defined as

$$l_{mag}(I) = \frac{1}{B_2^{ss}(I)} \int_{-\infty}^{+\infty} B_2(I, z) dz. \quad (3)$$

Integrated field harmonics as defined in equation (1) are summarized in Table VIII for the case of the short model (MQXF) and the full length magnets. Only the harmonics order where the contribution of the ends is greater than 0.1 unit is reported in the table.

TABLE VIII: INTEGRATED FIELD HARMONICS

units at $R_{ref}=50$ mm	$\bar{b}_6$	$\bar{b}_{10}$	$\bar{a}_2$	$\bar{a}_6$
2D	0.7	-0.4	0	0
3D-MQXFS (1.2 m)	9.5	-0.5	-8.9	0.6
3D-LARP-MQXFL (4.2 m)	3.3	-0.4	-2.7	0.2
3D-CERN-MQXFL (7.15 m)	2.3	-0.4	-1.6	0.1

As can be observed, there is a non-negligible contribution to the average  $b_6$  and  $a_2$ . This is mainly due to the contribution of the layer jump and the current leads in the splice extension region. To compensate for this, a second 2-D coil optimization will be performed. In order to show the local contribution of the ends to the integrated field, Fig. 16 shows the pseudo-harmonics  $b^*_n$ , defined as:

$$b^*_n(z) = \frac{\int_{z-\Delta z/2}^{z+\Delta z/2} B_n(z) dz}{B_2^{ss} \Delta z} \quad (4)$$

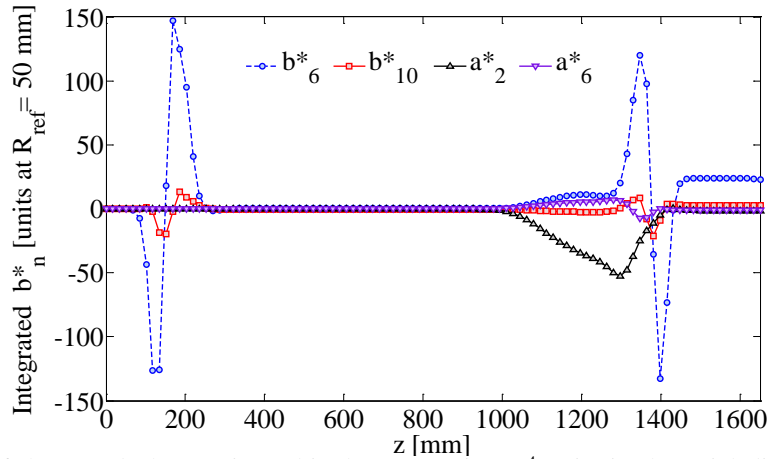


Fig. 16. Variation of the pseudo harmonic multipole content in  $10^{-4}$  units in the axial direction computed in ROXIE. Multipoles computed at a reference radius of 50 mm for a magnetic length of 1.2 m (MQXFS).

#### 4.4. MAGNETIC AND PHYSICAL LENGTHS

Table IX summarizes the magnetic and physical lengths of the coil, pad and yoke for MQXFS, for the 4.2-m length magnet (Q1/Q3) and for the 7.15-m length magnet (Q2a/Q2b).



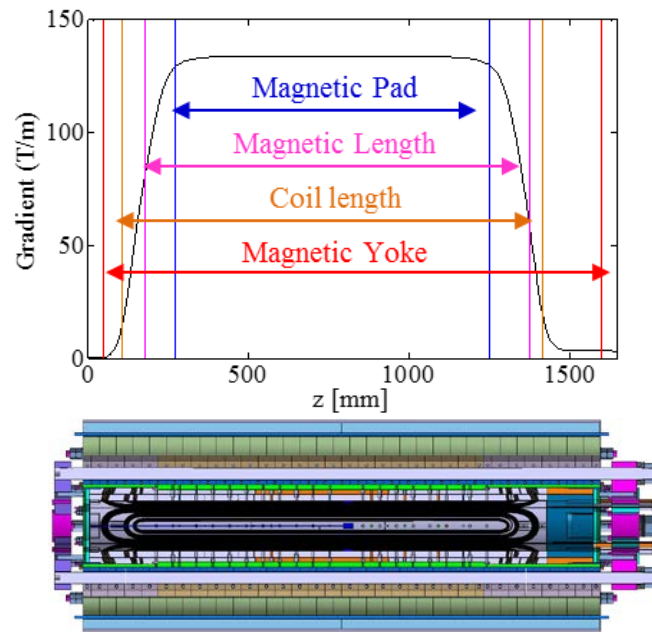


Fig. 17. Gradient as a function of the length for MQXFS for nominal current (16479 A)

TABLE IX: MAGNETIC LENGTH AND PHYSICAL LENGTHS

Parameters	Units	MQXFS	Q1/Q3	Q2
Magnetic length at 1.9 K	mm	1194	4200	7150
Coil length (from conductor to conductor)	mm	1313	4323	7282
Overall coil length (including splice extension)	mm	1510	4523	7481
Magnetic yoke extension	mm	1550	4563	7521
Magnetic pad extension	mm	975	3979	6946

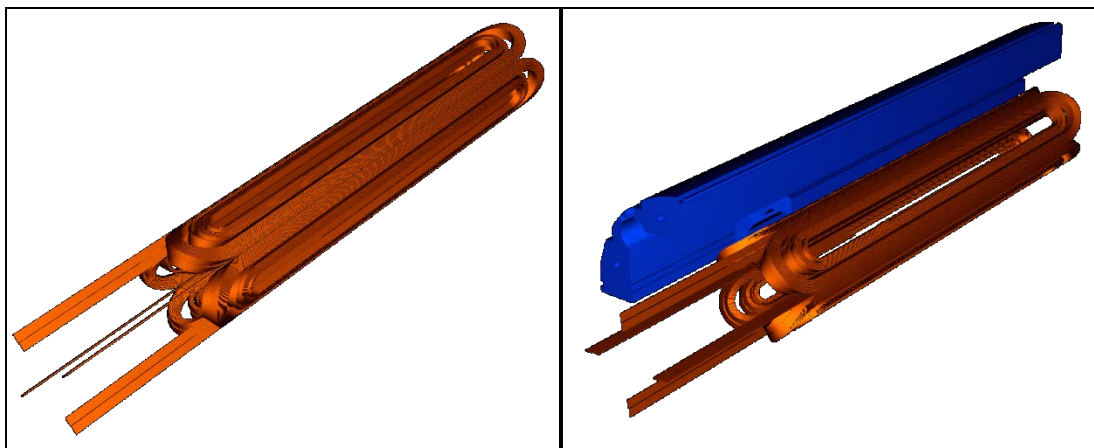


Fig. 18. 3D view of MQXFS coil

Fig. 17 shows the gradient as a function of the magnet length and a cut of the short model including coil and structure. Fig. 18 shows a 3D view of the coil and the magnetic structure.

## 5. COIL DESIGN AND PARTS

The coil fabrication technology is based on past LARP experience (TQ, LQ, HQ, LHQ coils) in order to reduce risks aiming at high coil yield. The MQXFS coil is a two-layer cos- $2\theta$  coil with saddle-shaped ends. The two-layer coil is wound continuously, without a splice at transition between the inner and outer layers, using the double-pancake technique successfully used in all LARP coils and by several other Nb<sub>3</sub>Sn magnets. The cross-section for magnetic design is shown in Fig. 19. The coil inner radius is 75 mm (i.e. the inner radius of the insulated cable at room temperature, without mechanical pre-load), and the outer radius is 113.13 mm. In order to ensure reaching the target dimensions, the coil size is controlled at each fabrication step. The coil model is shown in Fig. 20. To meet the requirement of a magnetic length of about 1.2 m for MQXFS1, the overall coil length will be 1.51 m. Due to the remaining pole gap, the coil length may vary from 1.510 m to 1.515 m. The coil consists of pole parts made of Ti-6Al4V, wedges made of phosphor bronze, and end parts made of SS 316. The MQXFS coil is wound around the pole. Fig. 21 shows the features of the inner and outer poles. Pole parts in each layer are aligned through the key stub, and pole parts between inner and outer layers are aligned through the pins. The poles are bolted to the winding anchor bars through clearances holes. The fabricated coil is lifted through lifting holes. Both clearance holes and lifting holes are designed with minimum 8 mm diameter and 50 mm spacing. These holes are also utilized as cooling channels to extract the heat from the coil aperture to the heat exchangers in the yoke. The wedge is fabricated through extrusion process to have the best uniform shape for each coil. Witness notches are added to each wedge for identification and orientation.

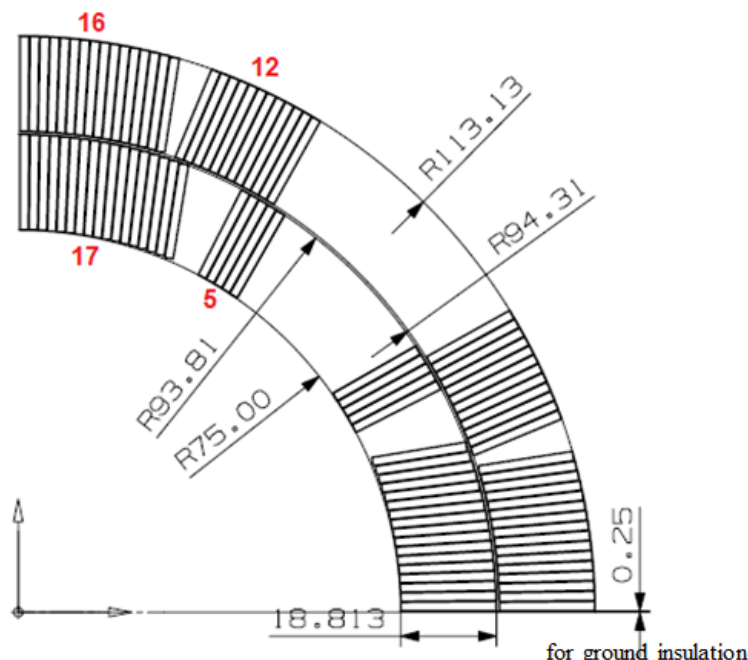


Fig.19 Coil Cross-section

End parts, saddles and splice block are designed based on the nominal coil size after reaction. End parts have been designed and optimized using BEND and ROXIE. After practice coils fabrication, the coil ends will be inspected and the final design will be decided. During winding, the coil is not fully constrained inside the envelope. This effect is most pronounced

at the ends. Prior to curing, the cable tries to separate from radial surface of the mandrel in some areas (spring-back), causing the shape of the turn not to match the shape of the end parts. The spring-back is larger with larger coil aperture and cable size. Therefore flexible features (slits) have been introduced in MQXF coil design (see Fig. 22). This is an incremental change with respect to single slit design previously used in LARP coils. For rapid prototyping the end parts are fabricated through laser sintering process. To simplify the requirement to bridge the slits during rapid prototyping the slits are EDM cut.

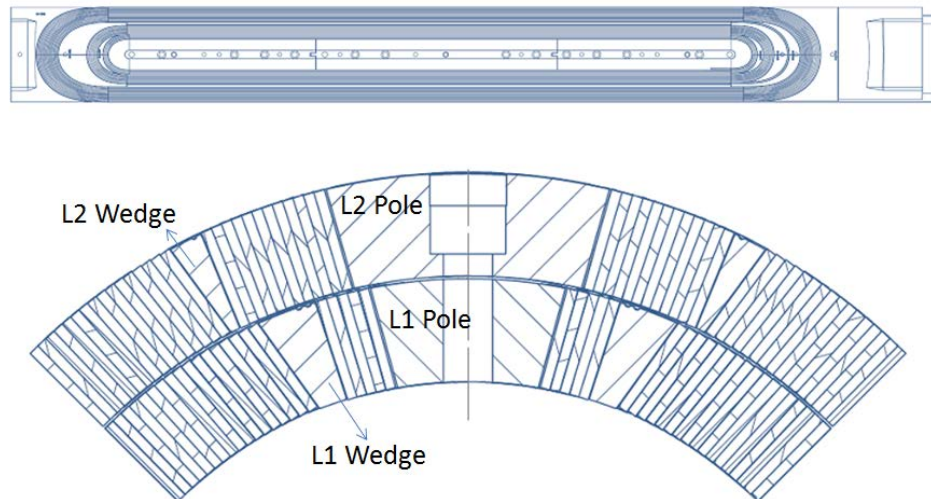


Fig. 20 MQXFS Coil Model

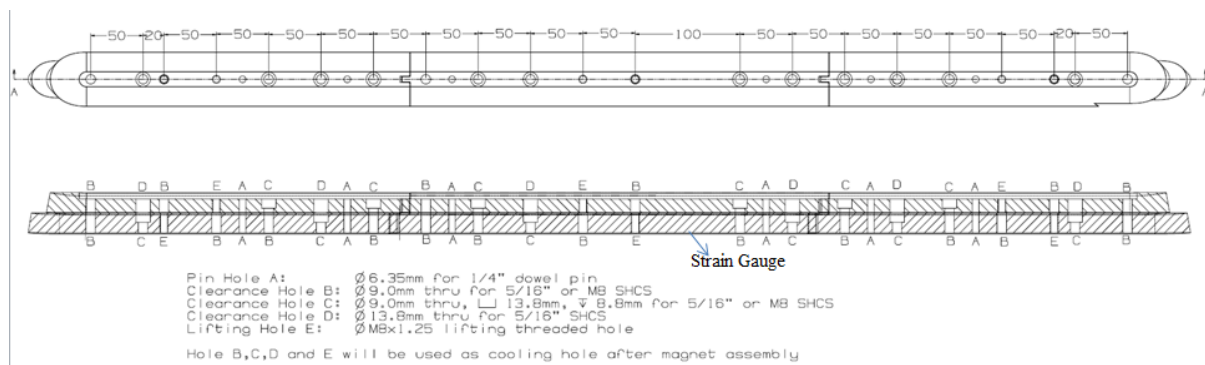


Fig. 21 Pole Parts Layout

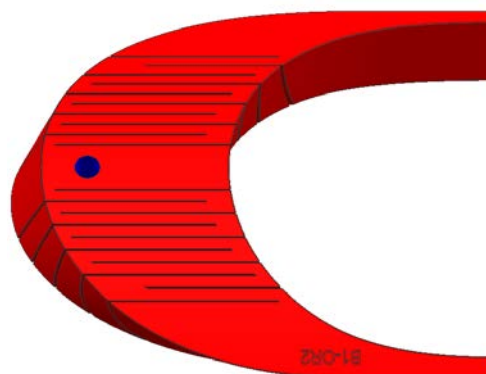


Fig. 22. Slits Design for End Parts

End parts are then plasma coated at 250  $\mu\text{m}$  thickness to increase the dielectric strength. The part number is then re-stamped into the part for clear identification.

## 6. STRUCTURE DESIGN AND INSTRUMENTATION

### 6.1. DESIGN CONCEPT

The support structure of MQXFS1 is made of three shell segments allowing for: (i) minimizing shell axial strain during cool-down and therefore the risk of stick-slip behaviour; (ii) reducing significantly shell fabrication cost; (iii) practicing with structure segment assembly in preparation for long prototypes and production magnets. The aluminium shells are pre-tensioned at room temperature with pressurized bladders. This cross-section is a direct scale-up of the HQ model. Fig. 23 shows the similarities between the two structures. The design comprises an iron yoke surrounded by a 29 mm thick aluminum shell, and includes four iron pads, four aluminum bolted collars and four coils wound around titanium poles. Between each pad and yoke two interference keys are used to balance the azimuthal tension in the outer shell with the azimuthal compression in the inner coils. The yoke, pads and collars are made of thick (50 mm) laminations assembled with tie rods. Previous experience on long magnets (LR and LQ) has shown the importance of segmenting the shell longitudinally. During cool-down, the shell contracts more than the iron yoke but the friction between shell and yoke prevents the shell from sliding axially, putting the shell in strong axial tension. During excitation, the shell might slip, leading to a change in azimuthal preload of the coils. In order to minimize axial tension in the shell and to ensure a uniform azimuthal load on the coil, the decision was made to segment the shell for long magnets.

The axial preload is provided by four 36-mm-diameter aluminum rods connected to a 75-mm-thick endplate which is connected to the coil end-saddles by mean of bullet screw. This system allows applying some axial preload at room temperature by pre-tensioning the rods with a piston. Final axial preload is applied after cool-down due to the shrinkage of the aluminum rods. In addition to the usual shell-based structure components, MQXFS1 structure includes alignment features.

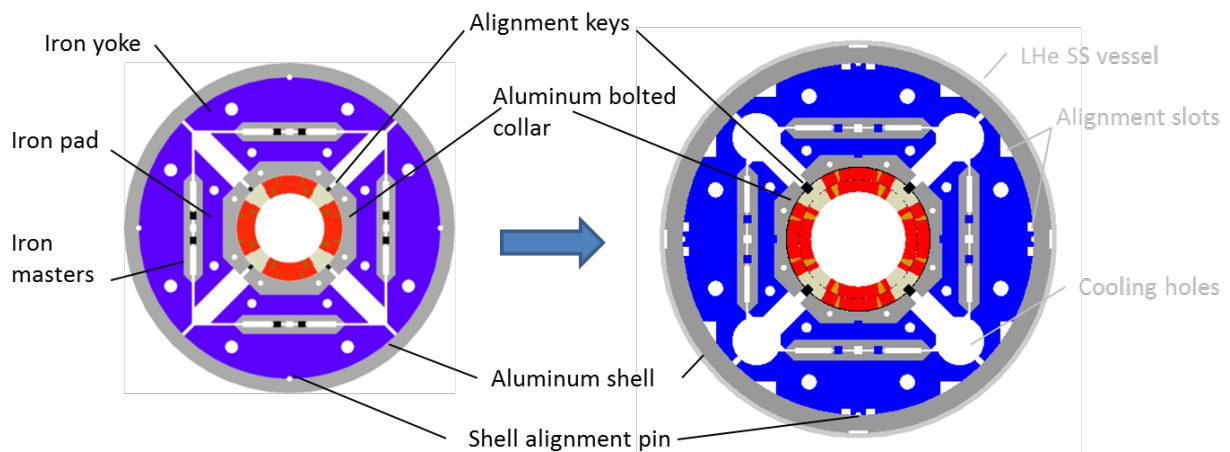


Fig. 23. Cross-section of HQ (left) and MQXFS1 (right)

The maximum outer diameter of the cold mass including its LHe vessel is limited by the

available space in the LHC tunnel and has been set by CERN to be 630 mm. Therefore, the outer diameter of the MQXFS1 structure is 614 mm (to be compared with the 570 mm of the HQ structure) allowing for an 8 mm thick LHe vessel. In addition, 77-mm-diameter holes providing room for heat exchanger have been added to the structure as seen on Fig. 23.

As shown in Fig. 23, alignment slot are incorporated at the mid-plane and at 45 degree. The mid-plane slots will accommodate a welding block which will be screwed to the yoke lamination. A backing strip will then be tack welded to the block. Let's note that the aluminum shell has a matching slot to accommodate the backing strip. In the case of a real LHe vessel assembly, a half stainless steel (SS) shell would be placed on top of the cold mass and tack welded to the backing strip. The assembly cold mass + half SS shell would then be rotated and another half shell would be placed on the magnet and welded to the first half shell, providing longitudinal LHe vessel. A 3D view of the assembly steps and of the ends is shown in Figs. 24 and 25.

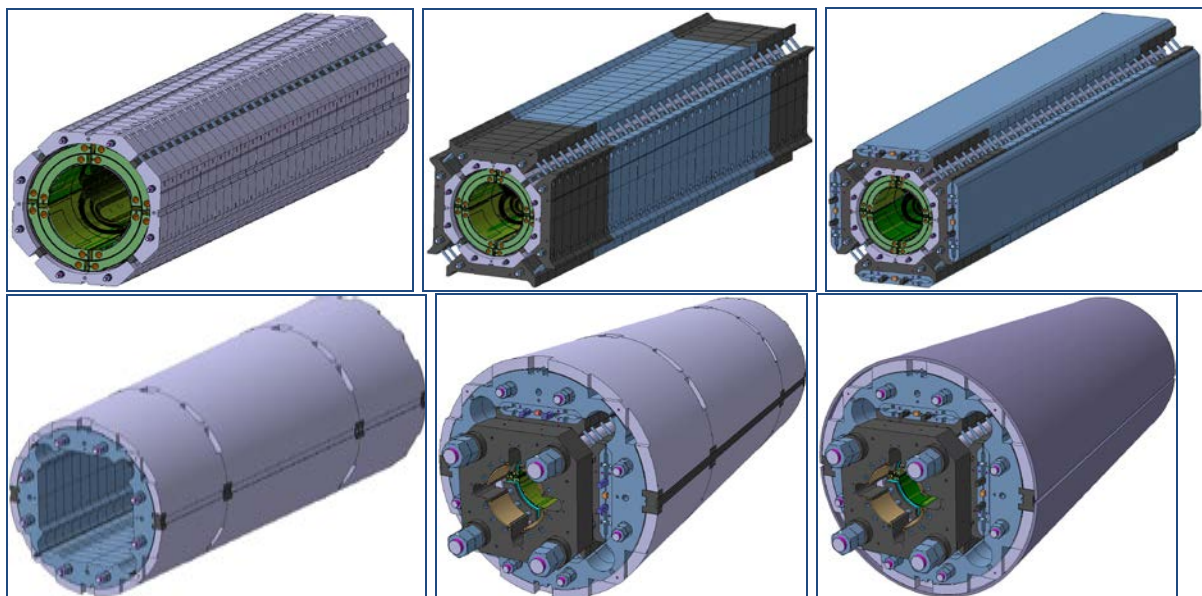


Fig. 24. Components of the MQXFS1 structure.

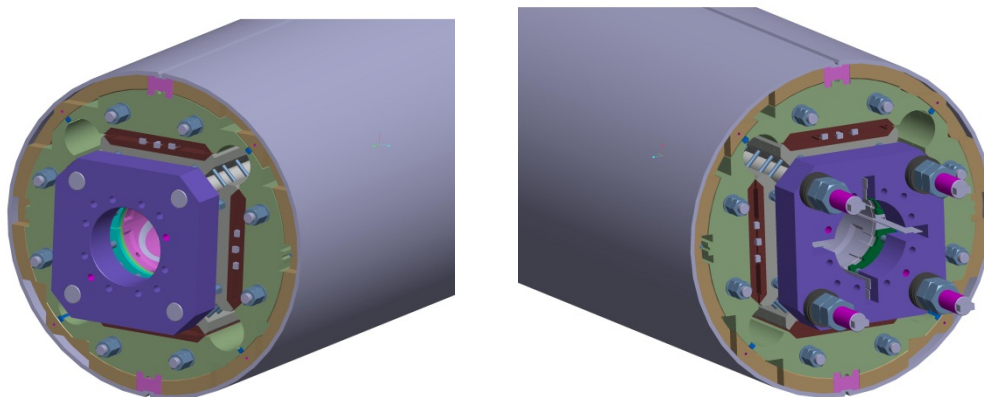


Fig. 25. MQXFS1 structure with endplate and axial rods (Return end on the left and Lead side on the Right)

## 6.2. 2D ANALYSIS

The finite element model of MQXFS includes friction and simulates 5 steps:

- Bladder inflated;
- Keys (bladder deflated);
- LHe vessel welding;
- Cool-down;
- Excitation: nominal (132.6 T/m) or ultimate gradient (143.2 T/m).

The purpose of the preload is to minimize coil motion during excitation. Ideally, the coil pole turn should remain in compression at all steps. Nevertheless, as we are dealing with Nb<sub>3</sub>Sn strain sensitive material, a trade-off has to be made between level of preload and peak stress reached in the conductor. A common solution is to allow some tension at the pole / coil interface of the order of 10 to 20 MPa at maximum gradient. This is achieved with an interference of 550 μm. Stress distribution is checked in the coil as shown in Fig. 26.

## 6.3. 3D ANALYSIS

### 6.3.1. Shell segmentation

As mentioned earlier, the shell requires segmentation to minimize the risk of uncontrolled slippage during excitation and in order to ensure homogeneous preload distribution.

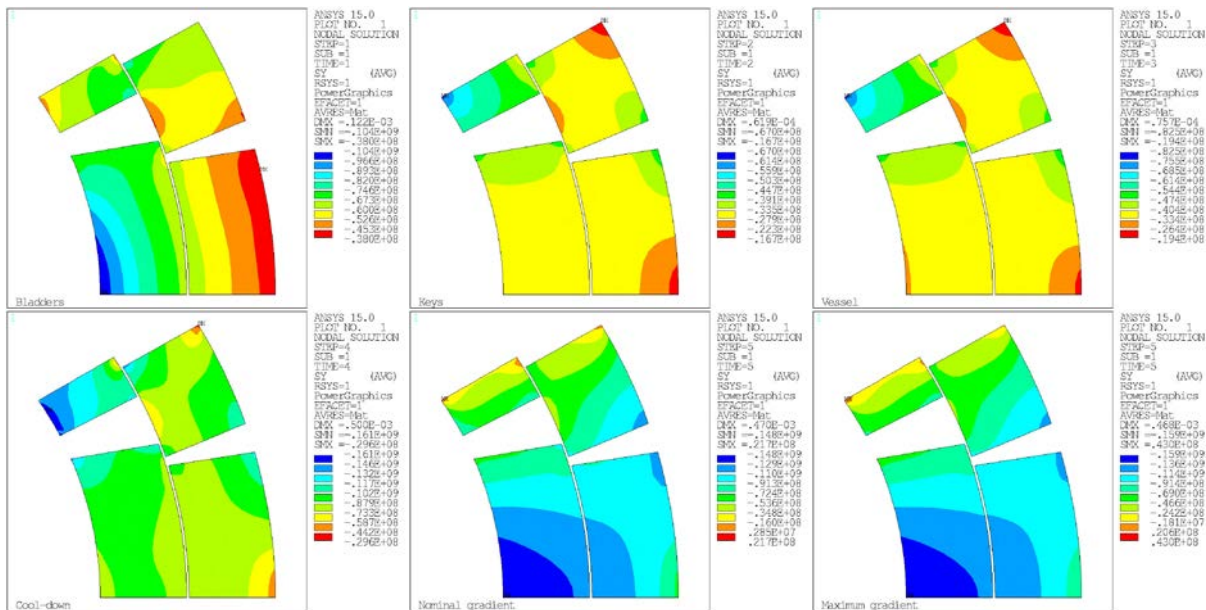


Fig. 26. Azimuthal stress distribution in the coil

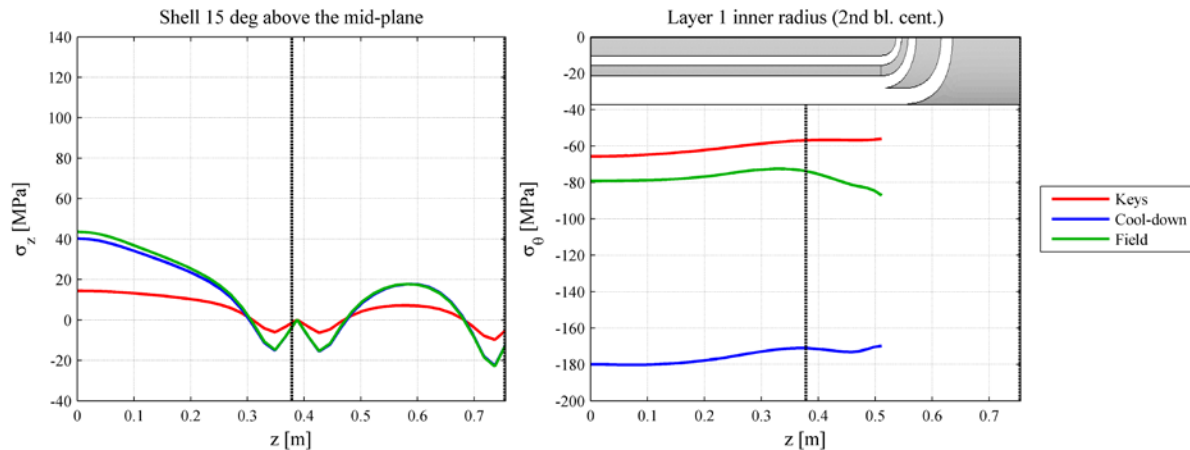


Fig. 27. Axial stress distribution in the shell (left) and azimuthal stress in the coil (right) in the case of a half-length shell covering the central part of the magnet and quarter-length shells covering the magnet extremities.

The numerical simulation led to the decision of setting the nominal MQXFS1 shell length to 774 mm (half-length shell segment). In order to reduce the coil stress in the lead and the return end, two shorter shells of the length of 387 mm (quarter-length shells) were introduced at the magnet extremities. Fig. 27 shows the axial stress in the final configuration of shell segments and the azimuthal stress in the coil at the location where the absolute stress levels are the highest.

## 6.4. MAGNET ASSEMBLY

The overall assembly process remains pretty consistent with the previous LARP magnets:

- Yoke-shell subassembly;
- Collar-pack assembly: the four coils are assembled in the bolted collars;
- Coil pack assembly: the collar-pack assembly is assembled in the bolted pads;
- Coil pack insertion in the yoke-shell subassembly;
- Rods and end-plate are positioned;
- Azimuthal (using bladders and keys) and axial (using rods and piston) preload is then applied.

Two MQXFS structures are being procured by CERN. One structure will be assembled at LBNL and one will be assembled at CERN. It is important to streamline the assembly process and to make it consistent between the two labs. Whereas the yoke-shell sub-assembly process does not have to be perfectly consistent, the coil assembly process in the collars and the remaining steps should follow the same procedure. Therefore work is presently done in both labs to converge on a common assembly procedure. As part of this work, the design of the assembly tooling is also ongoing. As part of the structure validation, the first assembly will be a mechanical model using instrumented aluminium dummy coils. This mechanical model will undergo a cold test in liquid nitrogen allowing checking the overall mechanical behaviour of the support structure.

## 7. QUENCH PROTECTION

The development of the quench protection system for the MQXF magnets is in progress and we plan using MQXFS1 as test bed for protection heaters developments and for the possible use of the CLIQ (Coupling-Loss Induced Quench) system [10]. The quench protection system for MQXFS1 aims at demonstrating the protection of the MQXF magnets in the LHC tunnel.

Therefore it is based on quench heaters on both inner and outer layers, and will explore the use of the CLIQ (Coupling Loss Induced Quench) system for MQXF magnets. In order to assess the impact of dynamic effects on the quench protection, a small dump resistor (providing the same L/R of the MQXFs in the tunnel at quench onset) will be used during MQXFS1 test. The quench heaters, made of 25  $\mu\text{m}$  thick stainless steel, are photo-etched on a 50  $\mu\text{m}$  thick polyimide sheet, which provides the coil-heater insulation together with the cable insulation (150  $\mu\text{m}$  S-2 glass impregnated with CTD-101k epoxy). The polyimide thickness is the result of a trade-off between high electrical strength and short heat-diffusion time.

Heaters on both inner and outer layers will be copper plated in order to minimize the time to quench the whole coil, since copper plating allows for closer heating stations in long coils. Several designs are under development and are planned to be tested on different coils.

The use of quench heaters on the inner layer is facing two challenges: (i) the polyimide layer should cover not more than 50%, or possibly less, of the coil surface in order to allow efficient heat transfer from the coil to the helium ring in the aperture; (ii) the layout of heaters and polyimide layer should prevent the formation of the so called “bubbles” (i.e. detachment of the heater from the coil and/or detachment of the insulation from the heater) seen in several LARP magnets with heaters or traces in the inner layer. Several techniques (punching, laser cuts) are being investigated for removing part of the polyimide sufficiently distant from the active trace elements. The most promising techniques will be used to make traces that will be tested with MQXFS1 coils.

Table X: Heater Design Parameters.

Peak power density	50-150 W/cm <sup>2</sup>
HFU voltage	up to 450 V
HFU current	up to 220 A
HFU capacitance	4.8-19.2 mF
Distance between heating stations	up to 120 mm
<b>Trace parameters</b>	
<i>Polyimide</i> Insulation thickness	50 $\mu\text{m}$
Stainless Steel thickness	25 $\mu\text{m}$
Copper thickness	10 $\mu\text{m}$
Glue thickness	up to 25 $\mu\text{m}$
Coil surface coverage by trace	< 50 % IL
Min distance btw trace elements and polyimide edge	7 mm or more

## 7.1. HEATER DESIGN

The set of heater design parameters, agreed upon by LARP and CERN, are provided in Table X. To improve quench protection redundancy and allow more freedom to experiment with heater powering during quench training, 6 individual heaters are placed on each coil: four for the outer layer and two for the inner layer side. The widths of the OL winding blocks are 31.74 mm and 23.74 mm, respectively, for the mid-plane and pole sections. The widths of the IL winding blocks are 30.75 and 9.19 mm correspondingly for the mid-plane and pole sections. Two designs have been proposed and are being implemented in the inner layer.

### 7.1.1. Copper-plated heater design 1 (IL)

Copper plating allows for scaling the heater length up to 6.7 m length and still permits the heater surface power to be above the design value of 150 W/cm<sup>2</sup>. Furthermore, to better



optimize heat deposition in the IL, the copper-plated bridges run across the wedge, while having heating stations only above the windings. The design is shown in Fig. 28.

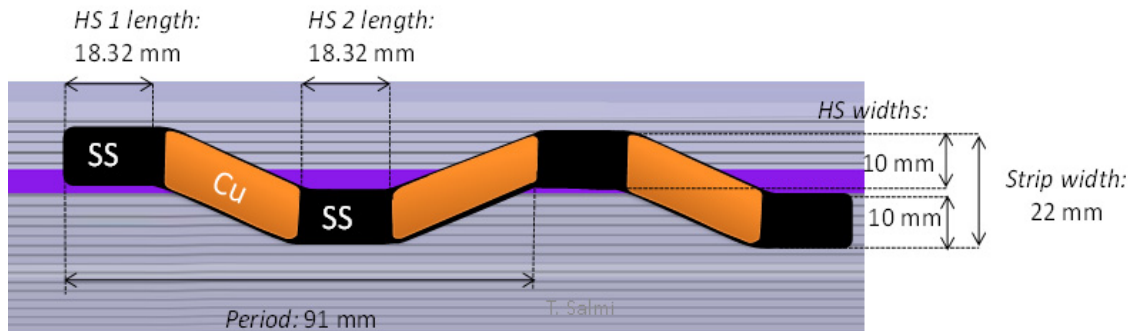


Fig. 28. “Snake” pattern for the inner layer heater layout. The copper-plated bridges run across the wedge separating two winding blocks, while heating stations are located within the winding blocks.

The main parameters of this layout are as follows:

Strip full span = 22 mm (leaving > 50 % free at the coil midplane), covering

- 4 turns on pole block (~7.2 mm);
- 5 turns on midplane block (~9.2 mm);
- Heating station (HS) width = 10 mm; length = 18.32 mm.

The optimization of the heating station length and period was conducted using “CoHDA” software by T. Salmi. A summary of heater design and operational parameters for the different MQXF lengths is given in Table XI.

Table XI. Summary of the IL heater parameters for the different QXF lengths

		Short	Q1/Q3	Q2
Magnet length	(m)	1	4	7
Heater width	(mm)	10	10	10
Heater thickness	(mm)	0.025	0.025	0.025
Station length	(mm)	18.3	18.3	18.3
Station distance	(mm)	72.7	72.7	72.7
Station resistance	(W)	0.0366	0.0366	0.0366
SS resistivity	(W m)	5.00E-07	5.00E-07	5.00E-07
Cu resistivity	(W m)	5.00E-10	5.00E-10	5.00E-10
Cu resistance	(W)	0.0002	0.0002	0.0002
Cu width	(mm)	9.4	9.4	9.4
Cu thickness	(mm)	0.01	0.01	0.01
Number of stations per turn		10	43	76
Total resistance	(W)	0.74	3.17	5.59
Voltage	(V)	59	253	448
Current	(A)	80	80	80
Power	(W/cm <sup>2</sup> )	128	128	128

### 7.1.2. Copper-plated heater design 2 (IL/OL)

As a next step towards heater optimization, another kind of the “snake” layout was proposed.

In this design, the copper-plated bridges are made narrower compared to the first copper-plated version. This should help improve heat transfer from the inner surface of the coils to the windings and allow for more spacing for perforations. Next, the heating station width is increased and they are brought farther apart azimuthally. Terminals of the heating stations are copper-plated to improve current flow uniformity. At the same time, for the outer layer, a set of simple straight strips was proposed that spans along the coil and across each (pole and mid-plane) winding block. The heating stations are the entire winding block. The heating stations are 40 mm in width and are separated by 120 mm long copper-plated bridges. The design layouts for both layers are shown in Fig. 29 and the summary of design and operational parameters for the different magnet lengths are summarized in Table XII.

Table. XII: Summary of the IL and OL heater parameters for the different QXF lengths

<b>QXF IL Parameters</b>		<b>short</b>	<b>US</b>	<b>CERN</b>
Magnet length	(m)	1	4	7
Heater width	(mm)	20	20	20
Heater thickness	(mm)	0.025	0.025	0.025
SS Station length	(mm)	25	25	25
Station period	(mm)	140	140	140
SS resistivity	( $\Omega$ m)	5.00E-07	5.00E-07	5.00E-07
Cu resistivity	( $\Omega$ m)	5.00E-09	5.00E-09	5.00E-09
Station resistance	( $\Omega$ )	0.0025	0.0025	0.0025
Cu resistance	( $\Omega$ )	1.13E-03	1.13E-03	1.13E-03
Cu thickness	(mm)	0.01	0.01	0.01
Cu width	(mm)	5	5	5
Number of stations		19	76	133
Total resistance	( $\Omega$ )	0.50	1.99	3.47
Voltage	(V)	99	397	521
Current	(A)	200	200	150
Power	(W/cm <sup>2</sup> )	200	200	112.5

QXF OL Parameters		short	US	CERN
Magnet length	(m)	1	4	7
Heater width	(mm)	20	20	20
Heater thickness	(mm)	0.025	0.025	0.025
SS Station length	(mm)	40	40	40
Station period	(mm)	160	160	160
SS resistivity	( $\Omega$ m)	5.00E-07	5.00E-07	5.00E-07
Cu resistivity	( $\Omega$ m)	5.00E-09	5.00E-09	5.00E-09
Station resistance	( $\Omega$ )	0.004	0.004	0.004
Cu resistance	( $\Omega$ )	0.003	0.003	0.003
Cu width	(mm)	20	20	20
Cu thickness	(mm)	0.01	0.01	0.01
Number of stations		8	32	56
Total resistance	( $\Omega$ )	0.34	1.38	2.41
Voltage	(V)	69	275	482
Current	(A)	200	200	200
Power	(W/cm <sup>2</sup> )	200	200	200

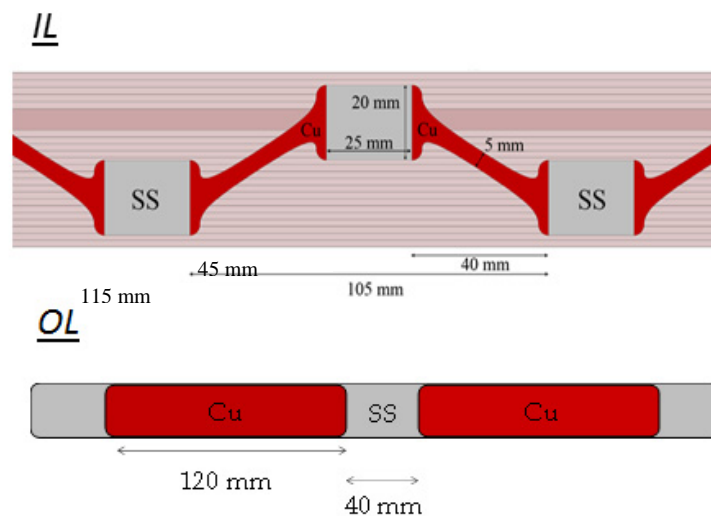


Fig. 29. The IL design features wide stainless heating stations connected by the narrower copper-plated bridges. The OL design is simplified to a set of two parallel strips running across the winding blocks, with periodic heating stations formed by copper plating.

## 7.2. TRACE FABRICATION

After the heaters have been designed they are drawn up in CAD, and the locations of the copper plating are also detailed. A negative mask of the trace elements is created, emulsion-side down, in order to mask off the areas for the photoresist. In the meantime, the SS/polyimide material is copper plated, using a nickel (Wood's Nickel process is most common) strike layer that helps to bond the 10  $\mu$ m of copper to the stainless steel. The trace fabrication process begins with lamination of the blank plated SS/polyimide material with a photoresist layer. The negative mask of the trace elements is then placed onto the photoresist

layer and exposed to UV light, which polymerizes the resist in areas that were not masked off. A washing process follows the exposure step in order to remove the unexposed resist from the SS/polyimide laminate. This patterned laminate is then etched in a ferric chloride solution, which removes both the copper and the stainless elements not protected by the hardened photoresist. A final washing step in this process removes the polymerized photoresist layer, which leaves the copper-plated trace elements on the polyimide. To selectively remove the copper layer from the stainless, a negative mask is generated and applied the same way as described above. Instead, however, of etching in a ferric chloride solution, the etchant solution is ammonium persulfate, which attacks only the copper layer. After all the washings, the resultant trace has the patterned elements with select copper-plated areas. The final step in the trace fabrication is to perforate the trace with a pattern of small holes, approximately 3 mm in diameter spaced about 10 mm apart, but leaving path lengths of  $>7$  mm to any metallic trace element. This requirement is for voltage standoff requirements. The inner layer traces should be perforated or cut in order to leave about 50% of the winding inner surface free from polyimide. This requirement is driven by the need for efficient heat extraction and by the need to avoid coil-trace delamination, commonly called “bubbles”. The first sets of inner layer traces are going to explore different techniques for removing the polyimide even if they will not achieve 50% free surface, which may require no voltage taps and adjustments to the heater design.

Prior to use in a coil, all instrumentation traces are tested at 3000 V to verify their electrical integrity.

### 7.3. CLIQ

MQXFS1 is going to explore and possibly demonstrate the use of CLIQ [10] for the protection of MQXF magnets. The CLIQ (Coupling-Loss Induced Quench) system was developed at CERN and successfully demonstrated for Nb3Sn magnets during the test of HQ02 [11]. MQXFS1 is going to have 3 special CLIQ leads coming out of the splice-connection box in order to accommodate different CLIQ configurations: single CLIQ unit, and double CLIQ unit. The double CLIQ unit configuration is expected to be the most efficient for long magnets because allows smaller voltages than the single CLIQ configuration. The test of MQXFS1 should demonstrate this advantage by reproducing the protection of full-length MQXF magnets through scaling of CLIQ voltages during MQXFS1 test. The CLIQ system is going to be tested on MQXFS1 in stand-alone mode and together with quench heaters on the outer layer.

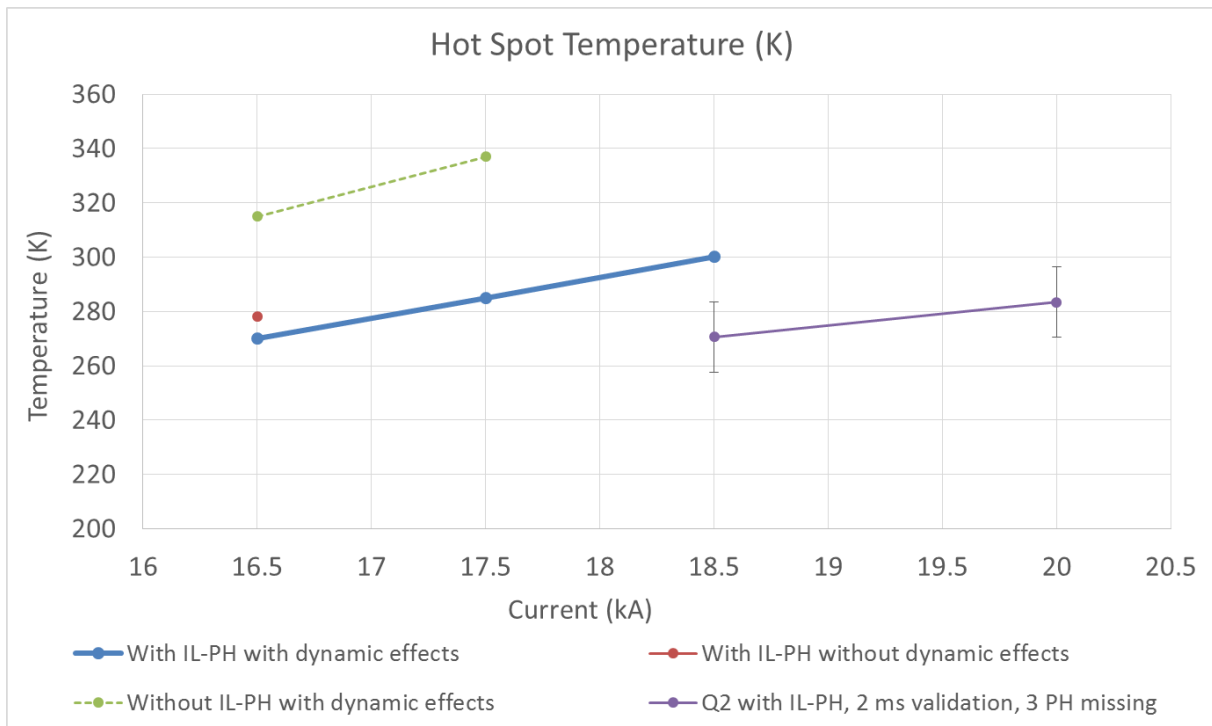


Fig. 30. Compute hot spot temperature as a function of current and in different protection system operations.

## 7.4. ANALYSIS

The quench analysis presented in this section was performed using the QLASA [12] code and the MATPRO [13] material property database. The main assumptions used for this analysis are:

- Operating current, 50 mΩ dump resistor on Q1 and Q3 in series, 10 ms validation time, 100 mV voltage threshold
- In all cases presented there are protection heaters installed on the Outer Layer (OL). The design of these OL heaters and their delays (16 ms - time between heater firing and quench start) are presented in [14]
- In case of no heaters on the inner layer the quench propagation from the outer to the inner layer is based on measurements (start of the quench in the inner layer) and conservative hypotheses (propagation within the inner layer does not take pre-heating into account)
- CLIQ has been simulated by assuming that the whole magnet is quenched after 10 ms (conservative assumption at 80% of SSL based on HQ tests)

In Fig. 30, the computed hot spot temperature is plotted as a function of the current and under different failure scenarios. At nominal current, so considering the operations in the tunnel, the peak temperature after a quench in Q2 (worst case scenario) is of 270 K with all the protection heaters working, and of 320 K when only the outer layer protection heaters are activated.

When CLIQ is also included (see Fig. 31), assuming diodes across each magnet and one CLIQ unit per magnet, the hot spot temperature reduces to 250 K if no protection heaters are utilized, and 230 K if CLIQ is combined to the outer layer heaters. Finally, the computed voltages in the various scenarios, and with and without CLIQ, are provided in Table XIII and XIV.

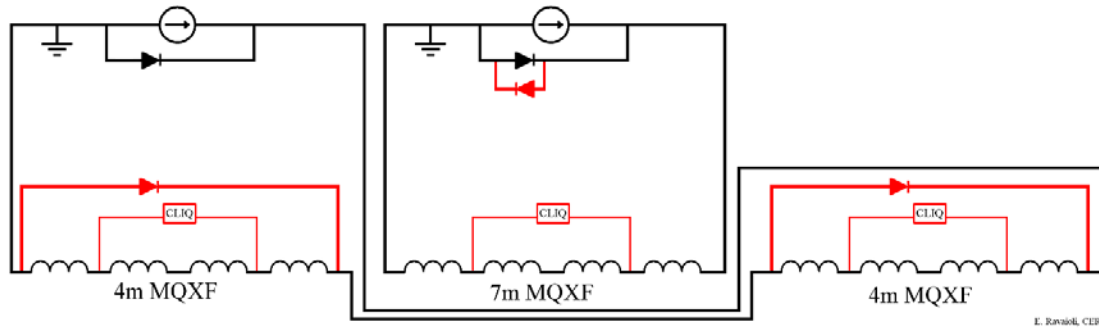


Fig. 31. Schematic view of implementation of CLIQ system to inner triplets, assuming diodes across each magnet and one CLIQ unit per magnet.

Table. XIII: Computed peak voltages

	Leads	Coil-Ground	Layer-layer	Mid-plane – Mid-plane	Turn-Turn
<b>Q1-Q3</b>	(V)	(V)	(V)	(V)	(V)
Nominal		970/570	201	151	24
OL heaters only	800	1152/752	265	151	39
HF-OL coil 1 heater fail	800	991/591	237	177	25
All coil 1 heaters fail	800	1571/1171	937	855	31
<b>Q2a-Q2b</b>	(V)	(V)	(V)	(V)	(V)
Nominal	800	667	273	335	37
OL heaters only	800	780	361	357	58
HF-OL coil 1 heater fail	800	661	394	319	40
All coil 1 heaters fail	800	1369	1481	1131	47

Table. XIV: Computed peak voltages with CLIQ

	Coil-Ground	Layer-layer	Mid-plane Mid-plane	Mid-planeIL Mid-planeOL	Turn-Turn
<b>Q2</b>	(V)	(V)	(V)	(V)	(V)
CLIQ + OL heaters	500	500	500	1000	35
CLIQ	530	500	500	1000	47

## 8. CONCLUSIONS

We presented the design for the inner triplet quadrupole based on the Nb<sub>3</sub>Sn technology. We presented the field quality analysis based on a four block coil, taking into account of the iron saturation and of coil heads. A second cross-section based on a cable with smaller keystone angle and a compensation of the different contributions aiming at zero multipoles at nominal current is planned after the construction of the first prototype. The mechanical structure is based on what has been developed for LARP TQ and HQ models, including all the features necessary for operation in the LHC. The protection is based on outer layer quench heaters, plus inner layer and/or CLIQ devices.

## References

- [1] O. Bruning, et al., LHC Design Report, CERN 2004-003 (2004).
- [2] S. Feher, et al., “Production and Installation of the LHC Low- $\beta$  Triplets,” *IEEE Trans. Appl. Supercond.*, vol. 16, no. 2, pp. 437-440, June 2006.
- [3] A. Yamamoto, et al., “Production and Measurement of the MQXA Series of LHC Low- $\beta$  Insertion Quadrupoles”, *IEEE Trans. Appl. Supercond.*, vol. 15, no. 2, pp. 1084-1089, June 2005.
- [4] S. Feher, et al., “Test results of LHC interaction regions quadrupoles produced by Fermilab,” *IEEE Trans. Appl. Supercond.*, vol. 15, no. 2, pp. 1090–1093, June 2005.
- [5] F. Borgnolutti, G. Ambrosio, S. Izquierdo Bermudez, D. Cheng, D. R. Dietderich, H. Felice, P. Ferracin, G. L. Sabbi, E. Todesco, and M. Yu, “Magnetic Design Optimization of a 150 mm Aperture Nb3Sn Low-Beta Quadrupole for the HiLumi LHC”, *IEEE Trans. Appl. Supercond.*, vol. 24, no. 3, June 2014, pp. 4000405.
- [6] S. Russenschuck, “Electromagnetic design and mathematical optimization method in magnet technology”, eBook Fourth Edition, ISBN: 92-9083-242-8, <http://russ.cern.ch/russ>.
- [7] A. Godeke et al., “A general scaling relation for the critical current density in Nb3Sn,” *Supercond. Sci. Technol.*, vol. 19, pp. R100-R116, 2006.
- [8] H. Felice, “Impact of coil compaction on Nb3Sn LARP HQ magnet,” *IEEE Trans. Appl. Sup.*, vol. 22, no. 3, June 2012.
- [9] P. Ferracin “Magnet Design of the 150 mm Aperture Low- $\beta$  Quadrupoles for the High Luminosity LHC”, *IEEE Trans. Appl. Supercond.*, vol. 24, no. 3, June 2014, pp. 4002306.
- [10] E. Ravaioli, et al., “New, Coupling Loss Induced, Quench Protection System for Superconducting Accelerator Magnets”, *IEEE Trans. Appl. Supercond.*, 24 500905.
- [11] E. Ravaioli, H. Bajas, V. I. Datskov, V. Desbiolles, J. Fevrier, G. Kirby, M. Maciejewski, G.L. Sabbi, H. H. ten Kate, A. P. Verweij, “Protecting a Full-Scale Nb3Sn Magnet with CLIQ, the New Coupling-Loss Induced Quench System”, *IEEE Trans. Appl. Supercond.*, early access: 10.1109/TASC.2014.2364892, 2014.
- [12] L. Rossi, M. Sorbi, “QLASA: a computer code for quench simulation in adiabatic multicoil superconducting windings”, INFN/TC-04/13, 2004.
- [13] G. Manfreda, L. Rossi, M. Sorbi, “MATPRO - Upgraded version 2012: a computer library of material property at cryogenic temperature”, INFN 12-04/MI, 2012.
- [14] T. Salmi, et al., “Protection Heater Delay Time Optimization for High-Field Nb<sub>3</sub>Sn Accelerator Magnets” *IEEE Trans on Applied Superc. Vol 23. No. 3*, June 2014.